

This is the accepted manuscript made available via CHORUS. The article has been published as:

## Role of Ion Kinetic Physics in the Interaction of Magnetic Flux Ropes

A. Stanier, W. Daughton, L. Chacón, H. Karimabadi, J. Ng, Y.-M. Huang, A. Hakim, and A. Bhattacharjee

Phys. Rev. Lett. **115**, 175004 — Published 21 October 2015

DOI: [10.1103/PhysRevLett.115.175004](https://doi.org/10.1103/PhysRevLett.115.175004)

# The role of ion kinetic physics in the interaction of magnetic flux-ropes

A. Stanier,\* W. Daughton, and L. Chacón  
*Los Alamos National Laboratory, Los Alamos, New Mexico 87545, USA*

H. Karimabadi  
*SciberQuest, Inc., Del Mar, California 92014, USA*

J. Ng, Y.-M. Huang, A. Hakim, and A. Bhattacharjee  
*Center for Heliophysics, Princeton Plasma Physics Laboratory, Princeton, New Jersey 08543, USA*  
(Dated: September 8, 2015)

To explain many natural magnetised plasma phenomena, it is crucial to understand how rates of collisionless magnetic reconnection scale in large magnetohydrodynamic (MHD) scale systems. Simulations of isolated current sheets concluded such rates are independent of system-size and can be reproduced by the Hall-MHD model, but neglect sheet formation and coupling to MHD-scales. Here, it is shown for the problem of flux-rope merging, which includes this formation and coupling, that Hall-MHD fails to reproduce the kinetic results. The minimum sufficient model must retain ion kinetic effects, which set the ion diffusion region geometry and give time-averaged rates that reduce significantly with system-size, leading to different global evolution in large systems.

Magnetic reconnection relaxes stressed magnetic fields, by changing field-line connectivity in highly conducting plasmas. The associated energy release is considered important for many magnetised plasma phenomena in nature [1, 2], but the theoretical question of how reconnection proceeds fast enough to explain this energy release in large systems is not fully understood.

Most of the previous simulation studies have addressed this question by initialising the simulations with isolated kinetic-scale current sheets, finding that the reconnection rate in collisionless plasmas is independent of both the system-size [3–6] and the mechanism that breaks the frozen-in condition, including specific details of the electron [7–9] and ion kinetic physics [10, 11] that are not present in two-fluid models. However, in nature, such current sheets take a finite time to form, and involve the interplay between magnetohydrodynamic (MHD) and kinetic scale physics. The magnetic island coalescence problem [12–16] is a simple reconnection test problem that includes many key features present in real systems: the build up of magnetic energy, dynamic formation of the current-sheet, and the on-set and the cessation of reconnection. Such islands are two-dimensional representations of magnetic flux-ropes, a fundamental building block of magnetised plasmas [17–19].

Reconnection during island coalescence is characteristically bursty, since it is coupled with the global motions of the islands, and thus it is suitable to consider the time averaged reconnection rate. A recent fully kinetic study [16] found that the average rate scales as  $\langle E_R \rangle \propto (\lambda/d_i)^{-1/2}$ , where  $d_i$  is the ion-skin depth and  $\lambda$  is the equilibrium current thickness, a proxy for the system size. However, no explanation for the strong system-size scaling has been given, and due to the computational difficulty of modelling large islands it has remained unclear how these predictions will compare with

the commonly used two-fluid models, such as Hall-MHD. Several studies [20, 21] have considered strongly driven Hall-MHD reconnection and reported significant system-size dependence, but impose an ad-hoc driving.

In this Letter, it is demonstrated that the Hall-MHD model fails to reproduce any of the key features from the equivalent fully-kinetic simulations of island coalescence: the peak and average reconnection rates, the dependence on the initial ion to electron temperature ratio  $T_{i0}/T_{e0}$ , the pile-up strength of the magnetic field, and the global island motion. In Hall-MHD, reconnection proceeds until the islands fully coalesce, and the peak and average rates have a weak dependence on system-size. In contrast, a hybrid model that retains kinetic ion physics with massless fluid electrons reproduces the broad ion diffusion region, and the associated reduction of the pile-up magnetic field and outflow velocity of the fully kinetic model. In hybrid and fully kinetic, reconnection in large systems is significantly slower, so that the islands bounce [12, 14] and have different global evolution to Hall-MHD.

The essential physics responsible for this discrepancy relates to the anisotropic and agyrotropic nature of the ion pressure tensor, in which a large contribution is due to the ion meandering orbits [11, 22, 23] within the weak magnetic field regions of the reconnection layer. These orbits give rise to large gradients in the ion pressure tensor, which are not treated correctly in current fluid models. While the existence of broader ion layers has been mentioned in the literature [9–11, 24–27], their importance has been missed due to the extensive use of highly-extended current sheets for the initial conditions. Here, it is shown that ion pressure tensor effects play a primary role in controlling the magnetic field pile-up and outflow velocity, and thus determine the reconnection rate and the global evolution of this system. These results have conceivable implications for real reconnecting systems in

which coupling of micro to macro-scale physics is important, such as the Earth's magnetosphere.

All of the simulations described are initialised with a magnetic island equilibrium [28], with similar parameters to a recent study [16]. The initial magnetic potential is

$$A_z = B_0 \lambda \ln [\cosh (x/\lambda) + \epsilon \cos (y/\lambda)], \quad (1)$$

where  $\epsilon = 0.4$  and  $B_0$  is the asymptotic field. For a thermal pressure balanced equilibrium, the density profile is

$$n = n_b + \frac{n_0 (1 - \epsilon^2)}{[\cosh (x/\lambda) + \epsilon \cos (y/\lambda)]^2}, \quad (2)$$

where  $n_b = 0.2n_0$  is the background density,  $n_0$  is the central Harris-sheet density enhancement in the limit  $\epsilon = 0$ , and the initial temperatures are constrained as  $T_{i0} + T_{e0} = B_0^2 / (2\mu_0 n_0 k_B)$ . The ratio of ion to electron current carrying velocities is set equal to the temperature ratio  $T_{i0}/T_{e0}$  to give an exact Vlasov equilibrium in the fully kinetic case, see e.g. Ref. [29]. The simulation domain is  $x \in [-\pi\lambda, \pi\lambda]$ ,  $y \in [-2\pi\lambda, 2\pi\lambda]$ . In this study, the system-size,  $\lambda/d_i$ , and the initial temperature ratio,  $T_{i0}/T_{e0}$ , are varied. Additional code specific parameters are: for Hall-MHD [30–32], zero electron inertia  $d_e = 0$ , resistivity  $\eta = 10^{-5} \mu_0 d_i v_{A0}$ , hyper-resistivity  $\eta_H = 10^{-4} \mu_0 d_i^3 v_{A0}$ , and ion-viscosity  $\mu = 10^{-2} m_i n_0 d_i v_{A0}$ ; for hybrid ([33], and references therein),  $d_e = 0$ ,  $\eta = 10^{-5} \mu_0 d_i v_{A0}$ ,  $\eta_H = 10^{-3} \mu_0 d_i^3 v_{A0}$  and ratio of ion plasma frequency to gyro-frequency  $\omega_{pi}/\Omega_{ci} = 2000$ ; and for fully kinetic Particle-In-Cell (PIC) [34], ratio of electron frequencies  $\omega_{pe}/\Omega_{ce} = 2$ , and mass-ratio  $m_i/m_e = 25$  ( $d_e = d_i/5$ ). The results discussed are not sensitive to these choices, e.g. of  $\eta_H$  or  $\omega_{p\{i/e\}}/\Omega_{c\{i/e\}}$ . For all codes, an initial sinusoidal magnetic perturbation of amplitude  $\delta B = 0.1B_0$  is used to start the merging [16]. A movie showing the evolution of the current density (colour scale) and magnetic flux during the merging for the  $\lambda = 10d_i$  simulation can be found in the supplementary material.

Figure 1 shows the reconnection rate  $E_R$  against global-Alfvén time,  $t/t_A = tv_{A0}/(4\pi\lambda)$ , from Hall-MHD, hybrid and fully kinetic simulations with  $\lambda = 5d_i$  and  $T_{i0} = T_{e0}$ . Here,  $E_R$  is calculated as in Ref. [16],

$$E_R = \frac{1}{v_{Am} B_m} \partial_t [A_{zX} - A_{zO}], \quad (3)$$

where  $A_{zX/O}$  is  $A_z$  evaluated at the  $X/O$  magnetic null point,  $B_m$  is the maximum initial field between the islands, and  $v_{Am} = B_m/\sqrt{n_0 \mu_0 m_i}$ .

The peak reconnection rate for the hybrid simulation ( $E_R = 0.455$ ) is in good agreement with the fully-kinetic PIC result (0.435), whereas the Hall-MHD run (0.805) over-estimates the peak rate by  $\approx 85\%$ . Additional runs (not shown) confirm the peak rates do not depend on electron-scale physics, but the late time rate ( $t/t_A \gtrsim 1.5$ ,

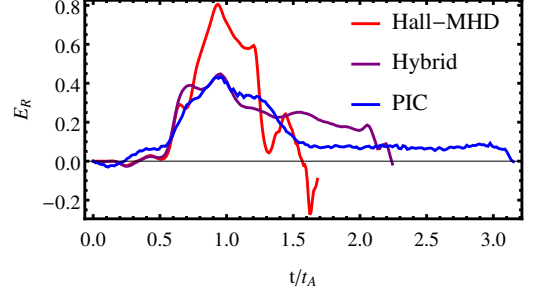


FIG. 1. Reconnection rate,  $E_R$ , against  $t/t_A$  for Hall-MHD (red), hybrid (purple) and fully-kinetic PIC (blue) runs with  $\lambda = 5d_i$  and  $T_{i0} = T_{e0}$ .

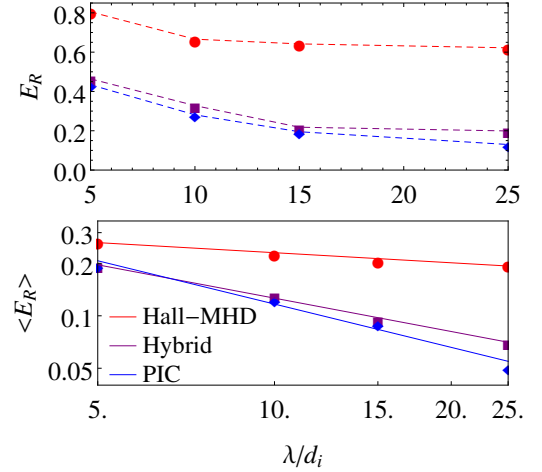


FIG. 2. Top: Peak rates ( $E_R$ ) against system-size ( $\lambda/d_i$ ) for Hall-MHD (red), hybrid (purple) and PIC (blue). Bottom: Average rates ( $\langle E_R \rangle$ ) over  $1.5\tau_A$ . The top (bottom) plot has linear (logarithmic) axes.

which differs between hybrid and PIC codes) does depend weakly on  $m_i/m_e$  in the PIC runs, or  $\eta_H$  for hybrid.

Figure 2 shows the peak rates,  $E_R$ , and the average rates,  $\langle E_R \rangle$  where  $\langle \rangle$  is the average over  $1.5\tau_A$  (chosen as a secondary island forms in the  $\lambda = 5d_i$  Hall-MHD simulation after this time, see below), against system-size,  $\lambda/d_i$ . In Hall-MHD,  $E_R$  flattens earlier ( $\approx 10d_i$ ) than hybrid and PIC runs, so the overestimate of  $E_R$  grows to more than a factor of three for  $\lambda = 25d_i$ . The average rates in hybrid,  $\langle E_R \rangle \propto (\lambda/d_i)^{-0.65}$ , and PIC,  $(\lambda/d_i)^{-0.8}$ , reduce significantly steeper with  $\lambda/d_i$  than Hall-MHD,  $(\lambda/d_i)^{-0.25}$ . This precise scaling with  $\lambda/d_i$  for the PIC runs differs from that reported in Ref. [16], and we find in general that these scalings depend on the aspect ratio of the simulation domain, which influences the dynamical interaction of the islands. Here, this aspect ratio is kept constant between all three codes as the system size is varied.

The differences in the rates have important consequences for the global evolution of the system. Figure 3

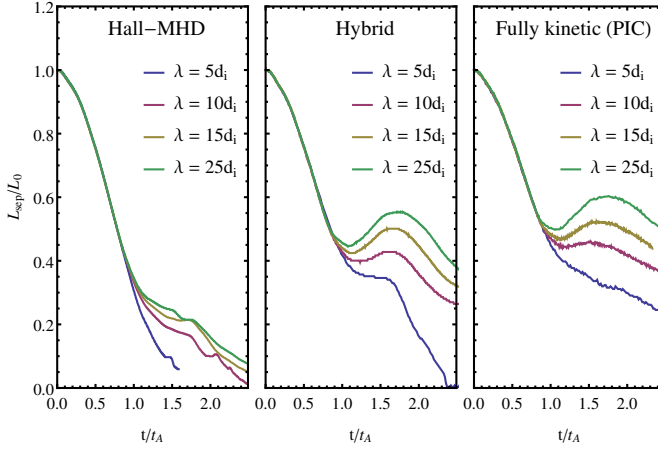


FIG. 3. Normalised O-point separation ( $L_{sep}/L_0$ ) against  $t/t_A$  for Hall-MHD (left), hybrid (middle) and PIC (right) runs. Shown for each code are system-sizes  $\lambda = 5d_i$  (blue),  $\lambda = 10d_i$  (pink),  $\lambda = 15d_i$  (gold), and  $\lambda = 25d_i$  (green).

shows the separation of the O-points, at the centre of the magnetic islands, normalised by the the initial separation  $L_0$  as a function of  $t/t_A$ . There are clear differences between the Hall-MHD and kinetic ion codes after the initial ideal phase  $t \gtrsim 0.8$ . For Hall-MHD (left panel) there is no clear reversal in the O-point separation, and the islands in these simulations tend to fully coalesce as they first approach each other. It must be noted that the  $\lambda = 5d_i$  run forms a secondary magnetic island at late time,  $t \approx 1.6$ , which stagnates reconnection and does cause the islands to bounce. However, since this bouncing is due to a separate issue, this evolution is not considered to compare fairly with the other runs. For hybrid and PIC, there is reversal in the O-point motion for system-sizes  $\lambda \geq 10d_i$ . The islands are unable to coalesce on the first approach due to the slower reconnection rates, and so bounce off each other. There is good agreement between hybrid and PIC, except for the late time  $t \gtrsim 2$  behaviour that depends on the electron scale physics, see above.

Figure 4 shows how the kinetic ion physics affects the geometry of the ion diffusion region. The  $z$ -component of the ion momentum equation can be expressed as an ion Ohm's law in normalised form,

$$E'_z = \frac{d_i}{n} [\partial_t (nv_{iz}) + \nabla \cdot (n\mathbf{v}_i v_{iz})] + \frac{d_i}{n} \nabla \cdot \mathbf{P}_{iz} + F_{coll,z}, \quad (4)$$

where  $E'_z = (\mathbf{E} + \mathbf{v}_i \times \mathbf{B}) \cdot \hat{\mathbf{z}}$  is the non-ideal electric field,  $\mathbf{P}_{iz} = \overline{\mathbf{P}_i} \cdot \hat{\mathbf{z}}$  is due to the ion-pressure tensor, and  $F_{coll,z} = \eta j_z - \eta_H \nabla^2 j_z$  is the resistive and hyper-resistive friction. When the right hand side of Eq. (4) is negligible the ideal-MHD Ohm's law is recovered, and the magnetic field is frozen-in to the ion fluid. However,  $E'_z$  becomes non-zero within the ion diffusion region, where the ion bulk flows decouple from the field. The contributions to

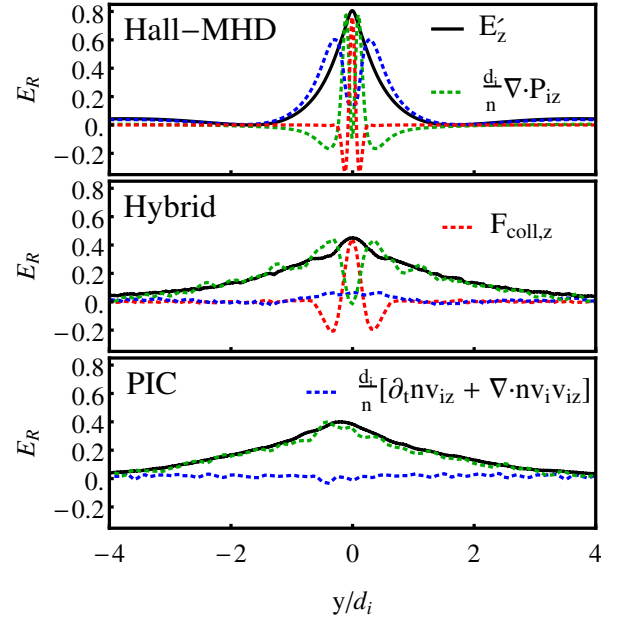


FIG. 4.  $E'_z$  (black) across the ion diffusion region ( $x = 0$ ) for Hall-MHD (top), hybrid (middle), and PIC (bottom) at peak  $E_R$ . Contributions from ion-inertia (blue), pressure tensor (green), and frictional terms (red). For all  $\lambda = 5d_i$ ,  $T_{i0} = T_{e0}$ .

$E'_z$  (black curves) in cuts across the ion diffusion region are shown in Fig. 4. For Hall-MHD (top) the thickness of the ion diffusion region, taken to be the full-width half-maximum of  $E'_z$ , is  $\delta_i = 0.62d_i$ .  $E'_z$  is primarily supported by bulk ion-inertia (blue dotted line), whereas ion pressure tensor effects (green) and frictional effects (red, mainly hyper-resistivity) are only significant very close to the X-point and so do not set the ion diffusion region thickness. For this Hall-MHD model,  $\mathbf{P}_{iz} = -\mu \nabla v_{iz}$  is a simple collisional ion-viscosity.

In contrast, the hybrid (middle) and PIC (bottom) have a broader ion diffusion region ( $\delta_i \approx 2.4d_i, 2.8d_i$  respectively), where the  $E'_z$  is primarily supported by gradients in the off-diagonal elements of the ion-pressure tensor (green). Here,  $\mathbf{P}_{iz}$  is collisionless and directly calculated from the distribution of ion particle velocities.

Figure 5 (top) shows the agyrotropy  $A\mathcal{O}_i$ , a scalar measure of the departure of  $\mathbf{P}_i$  from cylindrical symmetry with respect to the magnetic field (see Appendix A of Ref. [35] for the full definition), from the hybrid run. In a cut across the inflow axis ( $x = 0$ ), there is significant agyrotropy  $A\mathcal{O}_i = 0.2$  that peaks at  $y = \pm 1.9d_i$  upstream of the X-point. Also shown (white solid) is the trajectory of a typical ion test-particle starting at  $(x, y) = (3.2, -3.76)$  with local thermal velocity, and advanced using the electromagnetic fields of the hybrid run. The ion exhibits “meandering-type” [7, 11, 22] crossing orbits with reversal points at  $y_r \approx \pm 2.2d_i$ , before it enters the outflow region and is magnetised. This distance is in agreement with both the region of significant inflow agyrotropy and

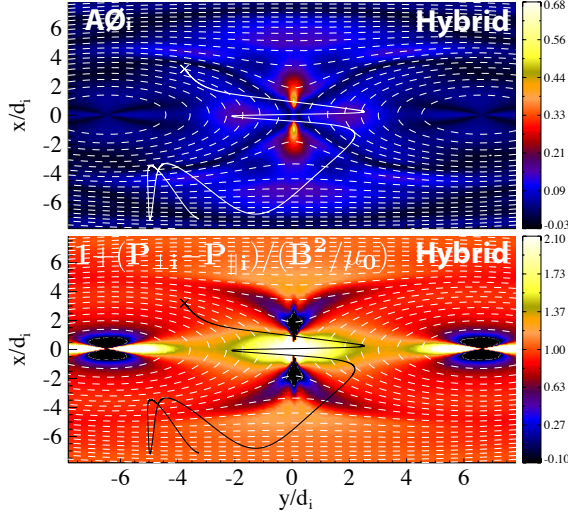


FIG. 5. Top: Ion agyrotropy,  $A\mathcal{O}_i$  (colour scale), flux contours (white, dashed) and ion test-particle orbit (white solid) starting from ‘x’ with thermal velocity. Bottom: Firehose parameter  $1 + (p_{i\perp} - p_{i\parallel})/(B^2/\mu_0)$  (colour scale), flux (white) and trajectory (black). From hybrid run with  $\lambda = 5d_i$ ,  $T_{i0} = T_{e0}$ .

the extent of the pressure tensor term in the ion Ohm’s law (middle panel of Fig. 4). Also of interest is the significant agyrotropy  $A\mathcal{O}_i \approx 0.6$  along  $y = 0$ , suggesting that non-gyrotropic pressure effects contribute to force-balance in the exhaust, but it is not as visible for large  $\lambda/d_i$  (not shown).

The reversal distance  $y_r$  and extent of regions with significant  $A\mathcal{O}_i$  decrease with  $T_{i0}$ , and decrease in proportion to the global system for larger  $\lambda/d_i$  (not shown). However, ion kinetic effects remain manifest on global scales via pressure anisotropy ( $p_{i\parallel}/p_{i\perp} \neq 1$ ). First, a wedge shaped pressure anisotropy region with firehose parameter,  $1 + (p_{i\perp} - p_{i\parallel})/(B^2/\mu_0) \gtrsim 1.3$  that is outside of  $y_r$  between the X and O-points in Fig. 5, is caused by perpendicular heating and coincides with the region of flux pile-up. Second, along  $y = 0$  the exhaust approaches the firehose instability threshold,  $1 + (p_{i\perp} - p_{i\parallel})/(B^2/\mu_0) \approx 0$ , reducing tension in the reconnected field and thus may reduce the outflows with respect to the inflow Alfvén speed (see below and Ref. [36]). The  $A\mathcal{O}_i$  and firehose parameter in PIC runs (not shown) agree well with hybrid.

Figure 6 shows the peak rate  $E_R$ , aspect-ratio  $\delta_i/w_i$ , inflow field  $B_{in,i}/B_m$  and outflow velocity  $v_{out,i}/v_{Am}$  from Hall-MHD, hybrid and kinetic runs with  $\lambda = 5d_i$ . Since  $y_r$  decreases with  $T_{i0}$ , the role of kinetic ions is studied by varying  $T_{i0}/T_{e0}$  in the hybrid simulations. Hall-MHD and PIC results are plotted for  $T_{i0}/T_{e0} = 1$ , although there is no noticeable temperature dependence in these quantities for Hall-MHD. For  $T_{i0}/T_{e0} = 1$ , Hall-MHD fails to reproduce  $E_R$ ,  $\delta_i/w_i$ ,  $B_{in,i}/B_m$ , or  $v_{out,i}/v_{Am}$  of the PIC runs, while hybrid captures all of these features reasonably well. As  $T_{i0}/T_{e0}$ , and thus  $y_r$ ,

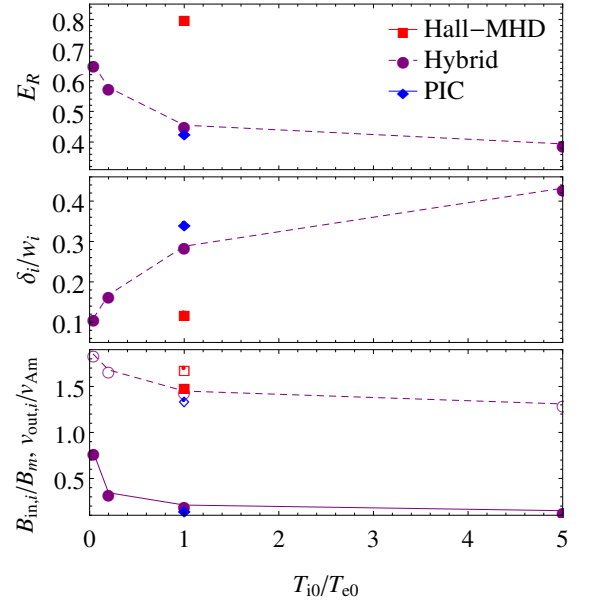


FIG. 6. Top: Peak rate  $E_R$ . Middle: Aspect-ratio of the ion non-ideal region,  $\delta_i/w_i$ . Bottom: Inflow field,  $B_{in,i}/B_m$  (hollow, dashed), and outflow velocity,  $v_{out,i}/v_{Am}$  (filled, solid). Results are from  $\lambda = 5d_i$  Hall-MHD (Red squares) and fully kinetic PIC (blue diamonds) with  $T_{i0}/T_{e0} = 1$ , and hybrid runs (purple circles) with  $T_{i0}/T_{e0} = 0.04, 0.2, 1, 5$ .

is reduced in the hybrid runs, it might be expected that Hall-MHD results are in better agreement. Indeed,  $\delta_i/w_i$  and  $B_{in,i}/B_m$  are closer to the Hall-MHD results, and the contribution to  $E'_z$  from ion-inertia becomes non-negligible (not shown). However, Hall-MHD still overestimates both  $E_R$  and  $v_{out,i}/v_{Am}$  with respect to the cold-ion hybrid, presumably as the hybrid ion pressure tensor does not remain cold or isotropic due to ion heating within the reconnection layer and outflow.

The magnetic island coalescence problem includes key features of real reconnecting systems: magnetic field pile-up, current sheet formation, and coupling between the MHD and kinetic scales. In this Letter, it is shown the widely used Hall-MHD fluid model is unable to reproduce such features from fully-kinetic PIC simulations. For this problem, kinetic ions are required to describe the structure of the ion pressure tensor, broader ion diffusion regions, pile-up magnitude, ion outflow velocity, and thus the reconnection rates and global behaviour of the PIC runs. The thickness of the ion diffusion region agrees with the extent of ion meandering orbits, and is associated with significant ion pressure agyrotropy and anisotropy. This physics is missing in Hall-MHD and work is presently being done to approximate such effects in more advanced fluid models [37, 38]. The importance of kinetic ions has been argued previously [26], but for an isolated current sheet the peak rate was similar to that in Hall-MHD. We also note that although electron kinetics

were not crucial for this problem, studies in Harris geometry have found them important to set the length of electron layers [36, 39], and can affect global behaviour through formation of secondary magnetic islands. The most important consequence of the present study is the different global evolution of the system between the Hall-MHD and kinetic ion codes. In Hall-MHD the islands fully coalesce on first approach, whereas hybrid and PIC islands with  $\lambda \geq 10d_i$  bounce off each other. The importance of such ion kinetic effects are conceivably generic to many real reconnecting systems where the coupling between macro to micro-scale physics is important.

This work is supported by NSF Grant No. AGS-1338944, and used resources provided by the Los Alamos National Laboratory Institutional Computing Program, which is supported by the U.S. Department of Energy National Nuclear Security Administration under Contract No. DE-AC52-06NA25396.

---

\* stanier@lanl.gov

- [1] E. Priest and T. Forbes, *Magnetic Reconnection* (Cambridge University Press, Cambridge, 2000).
- [2] E. G. Zweibel and M. Yamada, *Annu. Rev. Astron. Astrophys.* **47**, 291 (2009).
- [3] M. A. Shay, J. F. Drake, B. N. Rogers, and R. E. Denton, *Geophys. Res. Lett.* **26**, 2163 (1999).
- [4] J. D. Huba and L. I. Rudakov, *Phys. Rev. Lett.* **93**, 175003 (2004).
- [5] W. Daughton and H. Karimabadi, *Phys. Plasmas* **14**, 072303 (2007).
- [6] A. Stanier, A. N. Simakov, L. Chacón, and W. Daughton, *Phys. Plasmas* **22**, 010701 (2015).
- [7] M. Hesse, K. Schindler, J. Birn, and M. Kuznetsova, *Phys. Plasmas* **6**, 1781 (1999).
- [8] M. A. Shay and J. F. Drake, *Geophys. Res. Lett.* **25**, 3759 (1998).
- [9] J. Birn, J. F. Drake, M. A. Shay, B. N. Rogers, R. E. Denton, M. Hesse, M. Kuznetsova, Z. W. Ma, A. Bhattacharjee, A. Otto, and P. L. Pritchett, *J. Geophys. Res.* **106**, 3715 (2001).
- [10] M. A. Shay, J. F. Drake, B. N. Rogers, and R. E. Denton, *J. Geophys. Res.* **106**, 3759 (2001).
- [11] R. Horiuchi and T. Sato, *Phys. Plasmas* **1**, 3587 (1994).
- [12] D. Biskamp and H. Welter, *Phys. Rev. Lett.* **44**, 1069 (1980).
- [13] J. C. Dorelli and J. Birn, *J. Geophys. Res. (Space Phys.)* **108**, 1133 (2003).
- [14] D. A. Knoll and L. Chacón, *Phys. Plasmas* **13**, 032307 (2006).
- [15] D. A. Knoll and L. Chacón, *Phys. Rev. Lett.* **96**, 135001 (2006).
- [16] H. Karimabadi, J. Dorelli, V. Roytershteyn, W. Daughton, and L. Chacón, *Phys. Rev. Lett.* **107**, 025002 (2011).
- [17] E. N. Parker, *Astrophys. J.* **174**, 499 (1972).
- [18] X. Sun, T. P. Intrator, L. Dorf, J. Sears, I. Furno, and G. Lapenta, *Phys. Rev. Lett.* **105**, 255001 (2010).
- [19] W. Daughton, V. Roytershteyn, H. Karimabadi, L. Yin, B. J. Albright, B. Bergen, and K. J. Bowers, *Nature Phys.* **7**, 539 (2011).
- [20] X. Wang, A. Bhattacharjee, and Z. W. Ma, *Phys. Rev. Lett.* **87**, 265003 (2001).
- [21] R. Fitzpatrick, *Physics of Plasmas* **11**, 937 (2004).
- [22] T. W. Speiser, *J. Geophys. Res.* **70**, 4219 (1965).
- [23] M. M. Kuznetsova, M. Hesse, and D. Winske, *J. Geophys. Res. (Space Phys.)* **105**, 7601 (2000).
- [24] L. Yin and D. Winske, *Phys. Plasmas* **10**, 1595 (2003).
- [25] H. Karimabadi, J. D. Huba, D. Krauss-Varban, and N. Omidi, *Geophys. Res. Lett.* **31**, L07806 (2004).
- [26] H. Karimabadi, D. Krauss-Varban, J. D. Huba, and H. X. Vu, *J. Geophys. Res. (Space Phys.)* **109**, A09205 (2004).
- [27] N. Aunai, G. Belmont, and R. Smets, *J. Geophys. Res. (Space Phys.)* **116**, A09232 (2011).
- [28] V. M. Fadeev, I. F. Kvabtskhava, and N. N. Komarov, *Nucl. Fusion* **5**, 202 (1965).
- [29] K. Schindler, *Physics of Space Plasma Activity* (Cambridge University Press, Cambridge, 2006).
- [30] L. Chacón, *JPCS* **125**, 012041 (2008).
- [31] L. Chacón, *Phys. Plasmas* **15**, 056103 (2008).
- [32] Y.-M. Huang, A. Bhattacharjee, and B. P. Sullivan, *Phys. Plasmas* **18**, 072109 (2011).
- [33] H. Karimabadi, B. Loring, P. O’Leary, A. Majumdar, M. Tatineni, and B. Geveci, in *Proceedings of the Conference on Extreme Science and Engineering Discovery Environment: Gateway to Discovery*, XSEDE ’13 (ACM, New York, NY, USA, 2013) pp. 57:1–57:8.
- [34] K. J. Bowers, B. J. Albright, L. Yin, W. Daughton, V. Roytershteyn, B. Bergen, and T. J. T. Kwan, *J. Phys.: Conf. Ser.* **180**, 012055 (2009).
- [35] J. Scudder and W. Daughton, *J. Geophys. Res. (Space Phys.)* **113**, A06222 (2008).
- [36] A. Le, J. Egedal, J. Ng, H. Karimabadi, J. Scudder, V. Roytershteyn, W. Daughton, and Y.-H. Liu, *Phys. Plasmas* **21**, 012103 (2014).
- [37] L. Wang, A. H. Hakim, A. Bhattacharjee, and K. Geraschewski, *Phys. Plasmas* **22**, 012108 (2015).
- [38] J. Ng, Y. M. Huang, A. Hakim, A. Bhattacharjee, A. Stanier, W. Daughton, L. Wang, and K. Geraschewski, *Phys. Plasmas* (Unpublished).
- [39] W. Daughton, J. Scudder, and H. Karimabadi, *Phys. Plasmas* **13**, 072101 (2006).